



CHORUS

This is the accepted manuscript made available via CHORUS. The article has been published as:

Phonon-Limited Mobility in

$$\frac{h}{2\pi m^*}$$
 Encapsulated

$$\frac{A}{B}$$
 Stacked Bilayer Graphene

Cheng Tan, Davoud Adinehloo, James Hone, and Vasili Perebeinos

Phys. Rev. Lett. **128**, 206602 — Published 17 May 2022

DOI: [10.1103/PhysRevLett.128.206602](https://doi.org/10.1103/PhysRevLett.128.206602)

Phonon limited mobility in h-BN encapsulated AB-stacked bilayer graphene

Cheng Tan,¹ Davoud Adinehloo,² James Hone,^{1,*} and Vasili Perebeinos^{2,†}

¹*Department of Mechanical Engineering, Columbia University, New York, 10027 New York, USA*

²*Department of Electrical Engineering, University at Buffalo,
The State University of New York, Buffalo, New York 14260, USA*

(Dated: February 16, 2022)

The weak acoustic phonon scattering in graphene monolayer leads to high mobilities even at room temperatures. We identify the dominant role of the shear phonon mode scattering on the carrier mobility in AB-stacked graphene bilayer, which is absent in monolayer graphene. Using a microscopic tight-binding model, we reproduce experimental temperature dependence of mobilities in high-quality boron nitride (BN) encapsulated bilayer samples at temperatures up to ~ 200 K. At elevated temperatures, the surface polar phonon (SPP) scattering from BN substrate contributes significantly to the measured mobilities of 15,000–20,000 cm^2/Vs at room temperature and carrier concentration $n \sim 10^{12} \text{ cm}^{-2}$. A screened SPP potential for a dual-encapsulated bilayer and transferable tight-binding model allows us to predict mobility scaling with temperature and bandgap for both electrons and holes in agreement with the experiment.

Graphene has enabled novel electronic devices with excellent electronic properties [1]. Graphene hexagonal boron nitride (BN) encapsulation allows device fabrication with the state of the art electrical performance [2, 3]. The weak acoustic phonon scattering leads to extraordinary high mobilities even at room temperatures, as shown experimentally [2, 4–9] and theoretically [10–14]. The high-energy optical phonons are not thermally excited at room temperatures and have minimal contribution to the scattering. However, the lower energy surface polar phonons (SPP) in polar substrates can scatter carriers in graphene [15–19] or carbon nanotubes [20, 21]. In multilayer graphene, the role of additional vibrational modes on electrical transport and superconductivity [22, 23] has not been fully understood.

In this letter, we report temperature-dependent mobility measurements of high-quality h-BN encapsulated AB stacked graphene bilayers at different bandgap values. The experimental data are used to fine-tune the electron-phonon model Hamiltonian parameters [24] and to revisit the screening model for the SPP scattering in dual-encapsulated 2D materials. The calculations reveal the dominant contribution to the scattering of the low energy shear phonon mode, corresponding to the layer’s lateral displacements relative to each other. A combination of the intrinsic phonon and SPP phonon (from the BN substrate) scatterings reproduces the observed room-temperature mobility values of 15,000–20,000 cm^2/Vs in AB stacked bilayers. The reported mobility values are significantly lower than the intrinsic phonon limited mobilities in graphene monolayer devices fabricated under similar conditions resulting in minimal impurity scattering.

Sample fabrication has been described elsewhere [25]. The AB-stacked bilayer transistors are encapsulated by

30 nm thick hexagonal boron nitride, as schematically shown in Fig. 1a. This device design allows independent variation of the bandgap and doping level in bilayer graphene [26, 27]. The mobility is measured using a six-terminal configuration, eliminating the contact resistance contribution. Ref. [25] shows that the ambipolar hydrodynamic regime determines the transport properties at low carrier densities. However, at high carrier densities, i.e., $n \gtrsim 10^{12} \text{ cm}^{-2}$, corresponding to the Fermi levels above 30 meV, the standard band theory applies for electrical transport description up to room temperatures [25], the regime of interest here.

The electron and hole mobilities are shown in Fig. 1b and 1c, respectively, for different bandgap values. The sources of the temperature dependence of the mobility include intrinsic and extrinsic phonons [15, 28] and temperature-dependent screening of the Coulomb impurity scattering [29, 30]. In the high-quality samples, the Coulomb impurity limited mobility is not a dominant scattering mechanism, and we neglect its temperature dependence in the data analysis. We solve the Boltzmann Transport Equation (BTE) numerically for the mobility [12, 31] as a function of temperature for different bandgap values, using electron-phonon scattering matrix elements discussed in detail below [32]. The results are compared with the experiment in Fig. 1b and 1c

To provide a microscopic theory for the phonon-limited mobility in bilayer graphene, we employ a first-neighbor tight-binding model with in-plane π -orbitals overlaps t , which depend on the distance r_{ij} between the atoms: $t(r_{ij}) = t_0 - g\delta r_{ij}$, where $t_0 = 3.1 \text{ eV}$ and $g = 5.3 \text{ eV/\AA}$ [33]. For the interlayer coupling, we use a long-range model applicable for twisted bilayer graphene [24]:

$$t_{ij} = t_{\perp} \exp\left\{\left(-\frac{r_{ij} - h_0}{\lambda_z}\right)\right\} \exp\left\{\left(-\left(\frac{\xi_{ij}}{\lambda_{xy}}\right)^{\alpha}\right)\right\}, \quad (1)$$

where $h_0 = 3.35 \text{ \AA}$ is the equilibrium interlayer distance and $\xi_{ij} = ((x_i - x_j)^2 + (y_i - y_j)^2)^{1/2}$ is the in-plane distance between the atoms. Parameters $\lambda_z = 0.6 \text{ \AA}$

* jh2228@columbia.edu

† vasilipe@buffalo.edu

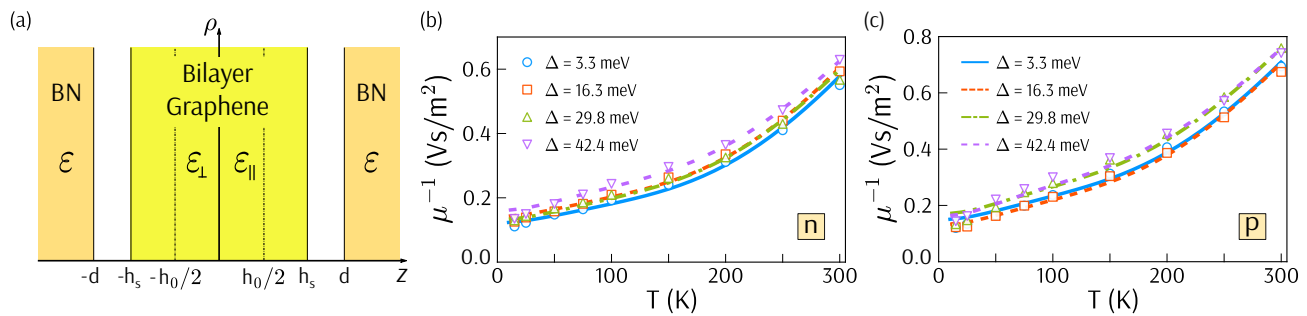


FIG. 1. (a) Schematic illustration of the device structure. Carbon atoms are located at $\pm h_0/2$. The temperature dependence of the inverse (b) electron and (c) hole mobilities for various bandgap values. The experimental data are shown by the marks and the BTE calculations by the lines, respectively. According to Matthiessens rule, the Coulomb limited mobilities given in table I were added to the calculated phonon-limited mobilities (see text).

and $t_{\perp} = 0.4$ eV are chosen to reproduce the interlayer distance dependence of the interband energy Δ_{12} (see Fig. 2a) from density functional theory (DFT), i.e., $d\Delta_{12}/dh_0 \sim \Delta_{12}/\lambda_z$ [24]. In the absence of the lateral screening, i.e., $\lambda_{xy} = \infty$, Eq. (1) would predict the separation between the two conduction bands of $\Delta_{12}(h = h_0) = 0.145$ eV unless a much smaller value of λ_z than the DFT value is used. That value of Δ_{12} is much smaller than a canonical value of ~ 0.4 eV [34, 35], consistent with the spectroscopic data [36]. We keep parameter $\lambda_{xy} = 1.7$ Å as in Ref. [24] and we adjust parameter α from the value of $\alpha = 1.65$ to $\alpha = 2.0$ to get a better match with the transport data in Fig. 1. The band structure is shown in Fig. 2a. The separation between the bands in our model is $\Delta_{12} = 0.36$ eV, as shown in Fig. 2a. Note that tight-binding models with interlayer hoppings described by several exponents [37, 38] also reproduce the DFT value of Δ_{12} .

The effective mass difference due to the electron-hole asymmetry in Fig. 2a translates to larger electron mobilities in agreement with the experiment. Our Hamiltonian Eq. (1) predicts $m_e = 0.030 m_0$ and $m_h = 0.035 m_0$, which matches well the available experimental values in the literature [39] with the correct sign for the electron-hole asymmetry, i.e., $m_h > m_e$. Note that the band structure masses do not include electron-electron renormalization, which reduces with increasing carrier density [40].

The phonons are calculated using an atomistic valence force model [41] for the in-plane interactions and the Lennard-Jones (LJ) 6-12 potential [42] between atoms in adjacent layers. The LJ parameters are determined by setting the van der Waals adhesion energy to $E_a = 60$ meV per atom [42] and interlayer spacing to $h_0 = 3.35$ Å. The shear mode energy of 32 cm^{-1} [43–45] is substantially underestimated in the LJ model. Therefore, we added a restoring force for the in-plane sliding distortions to the atomic potential to match the experimental shear mode energy [43–45]. The resulting phonon dispersions are shown in Fig. 2b.

We find that the intrinsic phonon scattering reproduces experimental mobilities reasonably well at temperatures

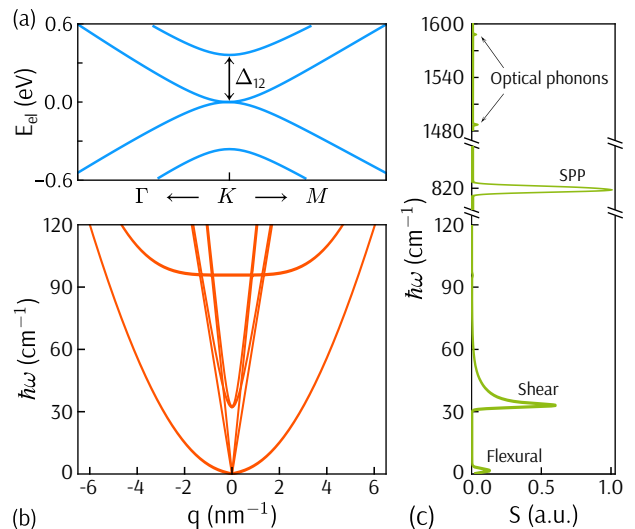


FIG. 2. (a) electronic band structure of AB-stack bilayer graphene with a zero bandgap. The band separation is depicted by Δ_{12} . (b) Phonon dispersion of the low energy phonons (from bottom to top at Γ point): flexural phonon, transverse and longitudinal acoustic phonons, doubly degenerate shear phonons corresponding to sliding in lateral directions, out-of-plane breathing phonon mode. (c) Normalized spectra function $S(\hbar\omega)$ from Eq. 9 at room temperature for n-doped bilayer with a gap of $\Delta = 3.3$ meV and concentration of $9 \times 10^{11} \text{ cm}^{-2}$. The integral of $S(\hbar\omega)$ gives the scattering rate, and integrals over specific energy windows give relative phonon contributions to scattering.

below 200 K. However, to account for the nonlinear temperature dependence in Fig. 1b and 1c at higher temperatures, we need to add SPP scattering from the h-BN phonons [12]. Following Ref. [46, 47], we extend the theory for the electron-SPP coupling in graphene structures on polar substrates [48] to dual-encapsulated bilayer graphene, shown in Fig. 1a. We look for a solution of Maxwell's equation for the spatial dependence of the electric potential due to the SPP phonon using the fol-

lowing ansatz [46]:

$$\varphi(\vec{\xi}, z) = \sum_{\vec{q}} \varphi(z) e^{i\vec{q}\cdot\vec{\xi}} \quad (2)$$

where \vec{q} is the in-plane 2D phonon wavevector and $\vec{\xi}$ is the in-plane vector. In isotropic materials, Poisson equation $\nabla\epsilon\nabla\varphi = 0$ requires that $\varphi(z) \propto e^{\pm q_z z}$ with out-of-plane wavevector q_z being equal to its in-plane counterpart, i.e., $q_z = |\vec{q}| = q$. However, in an isotropic dielectric material with $\epsilon_{\parallel} \neq \epsilon_{\perp}$, Poisson's equation solution requires that $q_z = q\sqrt{\epsilon_{\parallel}/\epsilon_{\perp}}$. Earlier papers on SPP scattering in graphene used unscreened SPP potential [12, 16, 17, 49], when the electron-SPP coupling is proportional to $\propto (1/(\epsilon_{\infty} + 1) - 1/(\epsilon_0 + 1))$, where ϵ_0 and ϵ_{∞} are low- and high-frequency dielectric constants of the polar substrate, respectively. The follow-up works accounted for screening by reducing the unscreened matrix element by ϵ_{\parallel} as in Ref. [50] or by employing more sophisticated calculations as in Ref. [51, 52].

Note that the electric field of the SPP mode is proportional to $\nabla\varphi$ and, hence, in an isotropic material, SPP electric field is tilted at 45° to the normal of the polar material. Therefore, it is natural to expect bilayer graphenes in-plane and out-of-plane dielectric constants to contribute to screening. To achieve that, we treat bilayer graphene as a finite width dielectric of thickness $2h_s$, as shown in Fig. 1a, where $h_s = h_0$ is an effective width of the electron π -orbitals. In perpendicular to the plane direction, we choose $\epsilon_{\perp} = 6$ appropriate for bilayer graphene interface [53]. For the in-plane direction, we choose static dielectric function $\epsilon_{\parallel} = 1 + v_c\Pi(q, k_F)$, where $v_c = 2\pi e^2/q$ is the Fourier transform of the Coulomb potential and $\Pi(q, k_F)$ is the polarization function which depends on carrier density n via the Fermi wavevector as $k_F = \sqrt{\pi n}$ at zero temperature. We use static, zero-temperature limit to evaluate $\Pi(q, k_F)$ in the Random Phase Approximation [54, 55].

The solution for $\varphi(z)$ has the form:

$$\varphi(z) = \begin{cases} \varphi_0 \cosh(qz) & |z| < h_s \\ A e^{q(z-d)} + B e^{-q(z-h_s)} & h_s \leq z < d \\ C e^{-q(z-d)} & d \leq z \end{cases} \quad (3)$$

where coefficients A , B , C and dispersion relation for SPP phonons are found using the boundary conditions: $\varphi^+ = \varphi^-$, $\epsilon^+ d\varphi^+/dz = \epsilon^- d\varphi^-/dz$ at $z = h_s$ and $z = d$, where superscripts “+” and “-” reflect corresponding functions to the right and to the left of the boundaries. The SPP dispersion is given by $\epsilon(\omega) = -\gamma(q)$, where $\gamma(q) = \gamma_1(q)/\gamma_2(q)$:

$$\begin{aligned} \gamma_1(q) &= \tanh(q(d - h_s)) + \sqrt{\epsilon_{\parallel}\epsilon_{\perp}} \tanh(qz h_s) \\ \gamma_2(q) &= 1 + \sqrt{\epsilon_{\parallel}\epsilon_{\perp}} \tanh(q(d - h_s)) \tanh(qz h_s), \end{aligned} \quad (4)$$

The BN dielectric function $\epsilon(\omega)$ is modeled as:

$$\epsilon(\omega) = \frac{\epsilon_{\infty}\omega^2 - \epsilon_0\omega_{TO}^2}{\omega^2 - \omega_{TO}^2}, \quad (5)$$

where $\epsilon_0 = 5.09$, $\epsilon_{\infty} = 4.575$, and $\hbar\omega_{TO} = 97.3$ meV [12, 56]. We omit the higher energy SPP phonon branch at ~ 200 meV. The resulting SPP dispersion is given by:

$$\omega_{SPP}(q) = \omega_{TO} \sqrt{\frac{\epsilon_0 + \gamma(q)}{\epsilon_{\infty} + \gamma(q)}}, \quad (6)$$

We find the constant φ_0 in Eq. 3 from the normalization condition [47, 48]:

$$\frac{1}{L^2} \frac{\hbar}{2\omega} = \int \frac{1}{4\pi} \frac{1}{2\omega} \left(\frac{\partial\epsilon}{\partial\omega} |\mathbf{E}_{\perp}|^2 + \frac{\partial\epsilon}{\partial\omega} |\mathbf{E}_{\parallel}|^2 \right) dr, \quad (7)$$

where $\mathbf{E}(\mathbf{r}) = -\nabla\varphi(\mathbf{r})$, $L^2 = N_k A_C$ is the sample area, A_C is the primitive two-atom unit cell area, and N_k is a number of k-points. Finally, the electron-SPP matrix element $M_{\mathbf{k}\mathbf{q}}$ can be obtained as

$$\begin{aligned} |M_{\mathbf{k}\mathbf{q}}|^2 &= (e\varphi_0)^2 |\langle \psi_{\mathbf{k}} | \psi_{\mathbf{k}+\mathbf{q}} \rangle|^2 \\ (e\varphi_0)^2 &= \frac{\pi e^2}{q A_C N_k} \hbar\omega \left(\frac{1}{\epsilon_{\infty} + \gamma(q)} - \frac{1}{\epsilon_0 + \gamma(q)} \right) f^2 \\ f^{-1} &= \cosh(qz h_s) \cosh(q(d - h_s)) \gamma_2(q), \end{aligned} \quad (8)$$

where $\gamma_2(q)$ is given by Eq. (4), ψ_k are single-particle wavefunctions. The inner product in Eq. (8) should be understood as the wavefunction overlap in a primitive unit cell, not the entire sample. In the low-energy model at zero gap, the wavefunction overlap is $|\langle \psi_{\mathbf{k}} | \psi_{\mathbf{k}+\mathbf{q}} \rangle|^2 = (1 + \cos(2\theta_{kk+q}))/2$, where θ_{kk+q} is the angle between the two wavevectors k and $k+q$ [57]. Note that the unscreened potential can be obtained by setting $h_s = 0$ in Eq. (8). The fast $1/q$ decay of the SPP matrix element suppresses large momentum scattering, such as intervalley and Umklapp scattering.

It is natural to expect that SPP scattering would double in dual-encapsulated devices since an SPP phonon can occur on either side in h-BN substrates. Indeed, this is the case in the limit of $qd \gg 1$. However, in the opposite limit $qd \ll 1$, the scattering matrix element is half of what one would expect in the case of bilayer transferred on h-BN with the top side exposed to air. We use $d = 1.5h_0$ as shown in Fig. 1a. The results of BTE simulations with intrinsic and SPP phonon scattering are shown in Fig. 1b and 1c together with the experiment. The Coulomb mobilities μ_C are added to the simulated phonon-limited mobilities μ_{ph} according to Matthiessen's rule [58]: $\mu^{-1} = \mu_{ph}^{-1} + \mu_C^{-1}$, where μ_C values are given in table I.

One way to identify phonon specific contributions to the scattering is to use a spectral function $S(\hbar\omega)$:

$$\begin{aligned} S(\hbar\omega) &= \sum_k \left(-\frac{\partial f_{0k}}{\partial E_k} \right) \sum_{q\mu} S_{kq}^{\mu} \frac{1 - f_{0k+q}}{1 - f_{0k}} \left(1 - \cos(\theta_{kk+q}) \right) \\ &\quad \times \delta(\hbar\omega - \hbar\omega_{-q\mu}) / \sum_k \left(-\frac{\partial f_{0k}}{\partial E_k} \right) \\ S_{kq}^{\mu} &= |\langle \psi_{\mathbf{k}} | H_{e-ph}^{\mu} | \psi_{\mathbf{k}+\mathbf{q}} \rangle|^2 [n_{-q\mu} \delta(E_{k+q} - E_k + \hbar\omega_{-q\mu}) \\ &\quad + (1 + n_{q\mu}) \delta(E_{k+q} - E_k - \hbar\omega_{q\mu})] \end{aligned} \quad (9)$$

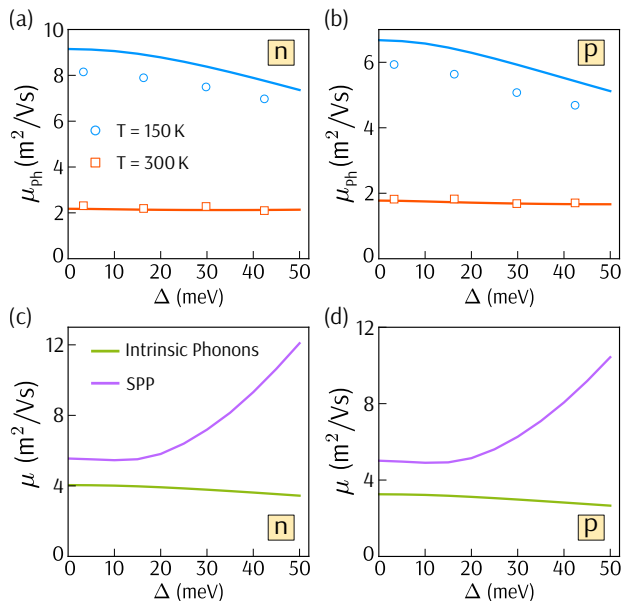


FIG. 3. Phonon-limited mobility for (a) electrons and (b) holes as a function of bandgap at room temperature and 150 K. The markers and solid curves represent experimental and theoretical mobilities, respectively. (c) and (d) depict room temperature mobilities calculated for one type of scattering in the Boltzmann Transport equation for electrons and holes, respectively.

where $\hbar\omega_{q\mu}$ are phonon energies with band index $\mu = 1 \dots 12$ for intrinsic phonons. For SPP phonons, the electron-phonon matrix element $|\langle\psi_k|H_{e-ph}^\mu|\psi_{k+q}\rangle| = |M_{\mathbf{kq}}|$ is given by Eq. (8). The electron-phonon Hamiltonian for intrinsic phonons is obtained by expanding Eq. (1) to linear order in the normal modes of phonon displacements. The equilibrium Fermi-Dirac distribution $f_{0k}(E_F - E_k, T)$ depends on temperature T and Fermi energy E_F . The Bose-Einstein phonon occupation number $n_{q\mu}$ depends on phonon energy $\hbar\omega_{q\mu}$ and temperature. The wavevector index k absorbs both wavevector direction and electron band index. The integral of $\int S(\hbar\omega)d\hbar\omega$ gives the scattering rate for the low-field transport [11, 13, 14]. The dominant contribution to the scattering of about 49% at room temperature comes from the shear phonon mode, as shown in Fig. 2c. The second-largest contribution comes from the SPP phonons of about 44%. The remaining 4% and 3% are contributed by the low energy flexural phonons and high energy (~ 200 meV) optical phonons. Note that relative contributions obtained from the analysis of function $S(\omega)$ in Eq. (9) are similar but not the same as those obtained from the full BTE solutions with the modified scattering rates discussed below.

The bandgap dependencies of the phonon-limited mobilities are shown in Fig. 3 together with the experimental mobilities corrected for the Coulomb impurity scattering according to Matthiessen's rule: $\mu_{exp}^{-1} - \mu_C^{-1}$, where μ_{exp} are the measured values shown in Fig. 1a and 1b,

| Δ (meV) | 3.3 | 16.3 | 29.8 | 42.4 |
|--------------------------------------|-----|------|------|------|
| μ_C^e (m^2/Vs) | 8.5 | 7.3 | 7.8 | 6.4 |
| μ_C^h (m^2/Vs) | 6.9 | 7.9 | 6.0 | 6.3 |

TABLE I. Impurity-limited mobilities for electrons and holes for various values of the bandgaps.

and μ_C values are given in table I. The nearly constant room temperature mobilities in Fig. 3a and Fig. 3b are in excellent agreement with the calculations for both electrons and holes. However, simulations using one type of phonon scattering show the opposite dependencies on the bandgap. The intrinsic phonon-limited mobility decreases with increasing bandgap, while the SPP mobility increases. The larger the density of electronic states at the Fermi level at larger bandgaps, the lower the intrinsic-phonon limited mobility. However, SPP mobility is determined by the density of final states at energies $E_F \pm \hbar\omega_{SPP}$. As the bandgap opens, the scattering involving phonon emission becomes suppressed due to the lack of the final states falling into the bandgap. As a result, the mobility increases with increasing bandgap roughly by a factor of two, as shown in Fig. 3c and Fig. 3d. At the small temperature of $T = 150$ K, the SPP scattering is suppressed due to the infinitesimal SPP phonon occupation number, and the experimental mobility demonstrates a decrease with increasing bandgap according to the theoretical predictions in Fig. 3a and Fig. 3b. Due to the long-range interaction of the tight-binding model Eq. 1, the electron-hole asymmetry in the band structure results in the systematically lower hole mobilities in agreement with the experiment.

In Fig. 4a, we demonstrate relative contributions to the total mobility from the SPP phonons, impurity scattering, and intrinsic phonons scattering. The latter has contributions from the shear, flexural, and residual contributions from the acoustic and optical phonons calculated when the electron-phonon contribution from the interlayer coupling in Eq. (1) is set to zero. The flexural and shear phonon contributions are calculated from the BTE solution with the electron-phonon coupling from the in-plane hopping matrix element distance dependence set to zero, i.e., in-plane $t(r_{ij}) = t_0$, and choosing appropriate phonon energies for scattering according to Fig. 2c. In Fig. 4a, the solid curve shows the BTE simulations, including all phonon scatterings, and it falls on top of the experimental data points after including Coulomb scattering using Matthiessens rule. The impurity scattering is assumed to be temperature independent.

The dashed curves in Fig. 4a show results of the BTE solutions with only one type of phonon scatterings. We find deviations of 10-20% in the mobility values using the BTE solution with all types of phonon scattering and those obtained from Matthiessen's rule using BTE mobilities from the individual types of scattering. Note that at the intermediate temperature of 150 K, the Coulomb impurity scattering is comparable to the phonon scatter-

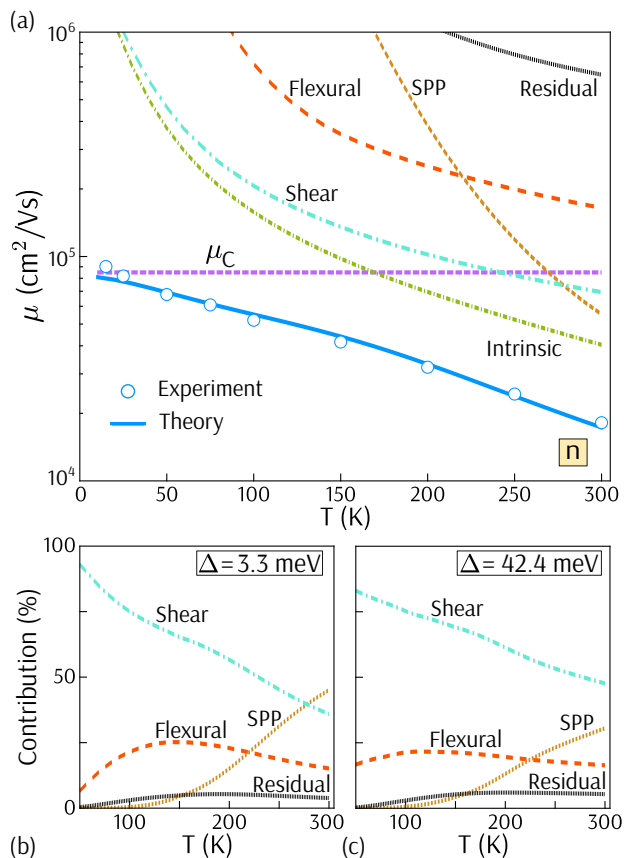


FIG. 4. (a) Overall experimentally measured and theoretically calculated electron mobilities as a function of temperature for n-doped bilayer with a gap of $\Delta = 3.3$ meV and concentration $9 \times 10^{11} \text{ cm}^{-2}$. The intrinsic, SPP, shear, flexural, and residual phonon-limited mobilities are shown by the dashed curves from bottom to top (at room temperature), respectively. (b) and (c) show relative phonon contributions to the total mobility as a function of temperature for $\Delta = 3.3$ meV and $\Delta = 42.4$ meV, correspondingly.

ing, unlike the case at room temperatures, when phonons dominate. Therefore, we expect an error introduced by Matthiessen's rule in extracting phonon-limited mobility from the experimental data at 150 K to be responsible for a larger discrepancy between the theory and the experiment in Fig. 3a and b. Finally, we implemented a tight-binding model from Ref. [38] for the intrinsic phonon scattering and found mobilities larger than reported here by only 20%.

In Fig. 4b and c, we show relative contributions of different phonon modes to the total phonon-limited mobility as a function of temperature for small and large bandgap bilayers, respectively. When the gap is large, the shear phonon dominates over an entire temperature range. SPP dominates at room temperature in a small gap bilayer, although the sum of all intrinsic phonons

overwhelms SPP contribution, which is consistent with Fig. 3c. In monolayer graphene, flexural phonons couple to electrons in the second-order perturbation theory [4, 8, 59], while in bilayer graphene, flexural phonons have non-vanishing electron-phonon coupling in linear order. According to Fig. 4a, if the SPP, shear, and flexural phonon scatterings were suppressed, then bilayer graphene mobility at room temperature would have fallen in the range of 500,000-1000,000 cm^2/Vs , consistent with the monolayer mobility calculations using the same model [12].

In conclusion, we have shown theoretically and experimentally that, at high carrier densities, intrinsic phonons and extrinsic h-BN SPP phonon scatterings are responsible for the temperature-dependent mobility in AB-stacked bilayer graphene. Using the long-range tight-binding model, we identified the dominant scattering mechanism due to the low energy shear phonon mode, corresponding to the layers sliding relative to each other. The shear phonon scattering is absent in monolayer graphene, which explains high mobilities in monolayer devices fabricated under similar conditions resulting in minimal Coulomb impurity scattering. At room temperatures, the second-largest scattering contribution is due to the h-BN SPP phonons. We developed a model for screened electron-SPP phonon scattering in dual-encapsulated structures.

Our findings resolve a decade-old question of why bilayers graphene mobility is systematically lower than that in monolayers. Our relatively simple electron-phonon models in Eq. (1) and (8) are transferable to other layered carbon structures and can be used to study superconductivity and electrical transport in twisted bilayer graphene or other carbon-based van der Waals heterostructures [60]. The shear phonons are generic to many other layered 2D materials [61], such as polar transition metal dichalcogenides, and their role in carrier mobility is largely unexplored.

ACKNOWLEDGMENTS

We gratefully acknowledge funding from the Vice President for Research and Economic Development (VPRED), SUNY Research Seed Grant Program, and computational facilities at the Center for Computational Research at the University at Buffalo (<http://hdl.handle.net/10477/79221>). The experimental work at Columbia was primarily supported by the National Science Foundation program for Emerging Frontiers in Research and Innovation (EFRI-1741660). Samples were fabricated at the Columbia Nano Initiative Shared Facilities. C.T. acknowledges support from a National Defense Science and Engineering Graduate (NDSEG) Fellowship: Contract FA9550-11-C-0028, awarded by the U.S. Department of Defense.

-
- [1] A. H. Castro Neto, F. Guinea, N. M. R. Peres, K. S. Novoselov, and A. K. Geim, The electronic properties of graphene, *Rev. Mod. Phys.* **81**, 109 (2009).
- [2] C. R. Dean, A. F. Young, I. Meric, C. Lee, L. Wang, S. Sorgenfrei, K. Watanabe, T. Taniguchi, P. Kim, K. L. Shepard, and J. Hone, Boron nitride substrates for high-quality graphene electronics, *Nature Nano* **5**, 722 (2010).
- [3] L. Wang, I. Meric, P. Y. Huang, Q. Gao, Y. Gao, H. Tran, T. Taniguchi, K. Watanabe, L. M. Campos, D. A. Muller, J. Guo, P. Kim, J. Hone, K. L. Shepard, and C. R. Dean, One-dimensional electrical contact to a two-dimensional material, *Science* **342**, 614 (2013).
- [4] S. V. Morozov, K. S. Novoselov, M. I. Katsnelson, F. Schedin, D. C. Elias, J. A. Jaszczak, and A. K. Geim, Giant intrinsic carrier mobilities in graphene and its bilayer, *Phys. Rev. Lett.* **100**, 016602 (2008).
- [5] X. Du, I. Skachko, A. Barker, and E. Y. Andrei, Approaching ballistic transport in suspended graphene, *Nature nanotechnology* **3**, 491 (2008).
- [6] K. I. Bolotin, K. J. Sikes, Z. Jiang, M. Klima, G. Fudenberg, J. Hone, P. Kim, and H. Stormer, Ultrahigh electron mobility in suspended graphene, *Solid state communications* **146**, 351 (2008).
- [7] K. I. Bolotin, K. J. Sikes, J. Hone, H. L. Stormer, and P. Kim, Temperature-dependent transport in suspended graphene, *Phys. Rev. Lett.* **101**, 096802 (2008).
- [8] E. V. Castro, H. Ochoa, M. I. Katsnelson, R. V. Gorbachev, D. C. Elias, K. S. Novoselov, A. K. Geim, and F. Guinea, Limits on charge carrier mobility in suspended graphene due to flexural phonons, *Phys. Rev. Lett.* **105**, 266601 (2010).
- [9] A. S. Mayorov, R. V. Gorbachev, S. V. Morozov, L. Britnell, R. Jalil, L. A. Ponomarenko, P. Blake, K. S. Novoselov, K. Watanabe, T. Taniguchi, and A. K. Geim, Micrometer-scale ballistic transport in encapsulated graphene at room temperature, *Nano Letters* **11**, 2396 (2011).
- [10] H. Suzuura and T. Ando, Phonons and electron-phonon scattering in carbon nanotubes, *Phys. Rev. B* **65**, 235412 (2002).
- [11] E. H. Hwang and S. Das Sarma, Acoustic phonon scattering limited carrier mobility in two-dimensional extrinsic graphene, *Phys. Rev. B* **77**, 115449 (2008).
- [12] V. Perebeinos and P. Avouris, Inelastic scattering and current saturation in graphene, *Phys. Rev. B* **81**, 195442 (2010).
- [13] K. Kaasbjerg, K. S. Thygesen, and K. W. Jacobsen, Unraveling the acoustic electron-phonon interaction in graphene, *Phys. Rev. B* **85**, 165440 (2012).
- [14] T. Sohler, M. Calandra, C.-H. Park, N. Bonini, N. Marzari, and F. Mauri, Phonon-limited resistivity of graphene by first-principles calculations: Electron-phonon interactions, strain-induced gauge field, and boltzmann equation, *Phys. Rev. B* **90**, 125414 (2014).
- [15] J.-H. Chen, C. Jang, S. Xiao, M. Ishigami, and M. S. Fuhrer, Intrinsic and extrinsic performance limits of graphene devices on SiO_2 , *Nature Nano.* **3**, 206 (2008).
- [16] S. Fratini and F. Guinea, Substrate-limited electron dynamics in graphene, *Physical Review B* **77**, 195415 (2008).
- [17] A. Konar, T. Fang, and D. Jena, Effect of high- κ gate dielectrics on charge transport in graphene-based field effect transistors, *Physical Review B* **82**, 115452 (2010).
- [18] K. Zou, X. Hong, D. Keefer, and J. Zhu, Deposition of high-quality hfo_2 on graphene and the effect of remote oxide phonon scattering, *Phys. Rev. Lett.* **105**, 126601 (2010).
- [19] T. Low, V. Perebeinos, R. Kim, M. Freitag, and P. Avouris, Cooling of photoexcited carriers in graphene by internal and substrate phonons, *Phys. Rev. B* **86**, 045413 (2012).
- [20] V. Perebeinos, S. V. Rotkin, A. G. Petrov, and P. Avouris, The effects of substrate phonon mode scattering on transport in carbon nanotubes, *Nano Letters* **9**, 312 (2009).
- [21] B. Chandra, V. Perebeinos, S. Berciaud, J. Katoch, M. Ishigami, P. Kim, T. F. Heinz, and J. Hone, Low bias electron scattering in structure-identified single wall carbon nanotubes: Role of substrate polar phonons, *Phys. Rev. Lett.* **107**, 146601 (2011).
- [22] Y. Cao, V. Fatemi, S. Fang, K. Watanabe, T. Taniguchi, E. Kaxiras, and P. Jarillo-Herrero, Unconventional superconductivity in magic-angle graphene superlattices, *Nature* **556**, 43 (2018).
- [23] M. Yankowitz, S. Chen, H. Polshyn, Y. Zhang, K. Watanabe, T. Taniguchi, D. Graf, A. F. Young, and C. R. Dean, Tuning superconductivity in twisted bilayer graphene, *Science* **363**, 1059 (2019).
- [24] V. Perebeinos, J. Tersoff, and P. Avouris, Phonon-mediated interlayer conductance in twisted graphene bilayers, *Phys. Rev. Lett.* **109**, 236604 (2012).
- [25] C. Tan, D. Y. Ho, L. Wang, J. Li, I. Yudhistira, D. A. Rhodes, T. Taniguchi, K. Watanabe, K. Shepard, P. L. McEuen, C. R. Dean, S. Adam, and J. Hone, Realization of a universal hydrodynamic semiconductor in ultra-clean dual-gated bilayer graphene, *arXiv:1908.10921* (2019).
- [26] Y. Zhang, T.-T. Tang, C. Girit, Z. Hao, M. C. Martin, A. Zettl, M. F. Crommie, Y. R. Shen, and F. Wang, Direct observation of a widely tunable bandgap in bilayer graphene, *Nature* **459**, 820 (2009).
- [27] J. Yan and M. S. Fuhrer, Charge transport in dual gated bilayer graphene with corbino geometry, *Nano letters* **10**, 4521 (2010).
- [28] W. Zhu, V. Perebeinos, M. Freitag, and P. Avouris, Carrier scattering, mobilities, and electrostatic potential in monolayer, bilayer, and trilayer graphene, *Phys. Rev. B* **80**, 235402 (2009).
- [29] M. Lv and S. Wan, Screening-induced transport at finite temperature in bilayer graphene, *Phys. Rev. B* **81**, 195409 (2010).
- [30] Q. Li, E. H. Hwang, and S. Das Sarma, Disorder-induced temperature-dependent transport in graphene: Puddles, impurities, activation, and diffusion, *Phys. Rev. B* **84**, 115442 (2011).
- [31] Y. Trushkov and V. Perebeinos, Phonon-limited carrier mobility in monolayer black phosphorus, *Phys. Rev. B* **95**, 075436 (2017).
- [32] We use two dimensional k-point mesh 1881×1881 of the Brillouin zone, the energy cut-off of ± 0.4 eV around the charge neutrality point. The delta-functions for energy conservation law are modeled using $\delta(x) = \exp(-x^2/\sigma^2)/(1 + \exp(x/k_B T))/(\sqrt{\pi}\sigma(1 +$

- $\exp((\sigma/(2k_B T))^2)$), where $\sigma = 6$ meV. This choice for numerical implementation of delta-function ensures that the detailed balance for transition rates $W_{k,k+q} = W_{k+q,k} \exp((E_k - E_{k+q})/k_B T)$ is satisfied exactly, even when $x = E_k - E_{k+q} - \hbar\omega_q \neq 0$.
- [33] V. Perebeinos, J. Tersoff, and P. Avouris, Electron-phonon interaction and transport in semiconducting carbon nanotubes, *Phys. Rev. Lett.* **94**, 086802 (2005).
- [34] D. S. L. A. Edward McCann and V. I. Fal'ko, The low energy electronic band structure of bilayer graphene, *Phys. J. Spec. Top.* **148**, 91 (2007).
- [35] E. McCann and M. Koshino, The electronic properties of bilayer graphene, *Reports on Progress in Physics* **76**, 056503 (2013).
- [36] K. F. Mak, C. H. Lui, J. Shan, and T. F. Heinz, Observation of an electric-field-induced band gap in bilayer graphene by infrared spectroscopy, *Phys. Rev. Lett.* **102**, 256405 (2009).
- [37] S. Fang and E. Kaxiras, Electronic structure theory of weakly interacting bilayers, *Phys. Rev. B* **93**, 235153 (2016).
- [38] X. Lin, D. Liu, and D. Tománek, Shear instability in twisted bilayer graphene, *Phys. Rev. B* **98**, 195432 (2018).
- [39] K. Zou, X. Hong, and J. Zhu, Effective mass of electrons and holes in bilayer graphene: Electron-hole asymmetry and electron-electron interaction, *Phys. Rev. B* **84**, 085408 (2011).
- [40] G. Borghi, M. Polini, R. Asgari, and A. MacDonald, Fermi velocity enhancement in monolayer and bilayer graphene, *Solid State Communications* **149**, 1117 (2009).
- [41] V. Perebeinos and J. Tersoff, Valence force model for phonons in graphene and carbon nanotubes, *Phys. Rev. B* **79**, 241409(R) (2009).
- [42] R. Zacharia, H. Ulbricht, and T. Hertel, Interlayer cohesive energy of graphite from thermal desorption of polyaromatic hydrocarbons, *Phys. Rev. B* **69**, 155406 (2004).
- [43] P. H. Tan, W. P. Han, W. J. Zhao, Z. H. Wu, K. Chang, H. Wang, Y. F. Wang, N. Bonini, N. Marzari, N. Pugno, G. Savini, A. Lombardo, and A. C. Ferrari, The shear mode of multilayer graphene, *Nat. Materials* **11**, 294 (2012).
- [44] R. He, T.-F. Chung, C. Delaney, C. Keiser, L. A. Jauregui, P. M. Shand, C. C. Chancey, Y. Wang, J. Bao, and Y. P. Chen, Observation of low energy raman modes in twisted bilayer graphene, *Nano Letters* **13**, 3594 (2013).
- [45] C. Cong and T. Yu, Enhanced ultra-low-frequency interlayer shear modes in folded graphene layers, *Nat. Comm.* **5**, 4709 (2014).
- [46] M. V. Fischetti, D. A. Neumayer, and E. A. Cartier, Effective electron mobility in si inversion layers in metal-oxide-semiconductor systems with a high- κ insulator: The role of remote phonon scattering, *Journal of Applied Physics* **90**, 4587 (2001).
- [47] M. A. Stroschio and M. Dutta, *Phonons in nanostructures* (Cambridge University Press, 2001).
- [48] I. Paradisanos, K. M. McCreary, D. Adinehloo, L. Mouchliadis, J. T. Robinson, H.-J. Chuang, A. T. Hanbicki, V. Perebeinos, B. T. Jonker, E. Stratakis, *et al.*, Prominent room temperature valley polarization in WS₂/graphene heterostructures grown by chemical vapor deposition, *Applied Physics Letters* **116**, 203102 (2020).
- [49] E. H. Hwang, R. Sensarma, and S. Das Sarma, Plasmon-phonon coupling in graphene, *Phys. Rev. B* **82**, 195406 (2010).
- [50] E. H. Hwang and S. Das Sarma, Surface polar optical phonon interaction induced many-body effects and hot-electron relaxation in graphene, *Phys. Rev. B* **87**, 115432 (2013).
- [51] Z.-Y. Ong and M. V. Fischetti, Theory of interfacial plasmon-phonon scattering in supported graphene, *Phys. Rev. B* **86**, 165422 (2012).
- [52] Z.-Y. Ong and M. V. Fischetti, Theory of remote phonon scattering in top-gated single-layer graphene, *Phys. Rev. B* **88**, 045405 (2013).
- [53] R. Bessler, U. Duerig, and E. Koren, The dielectric constant of a bilayer graphene interface, *Nanoscale Adv.* **1**, 1702 (2019).
- [54] E. H. Hwang and S. Das Sarma, Screening, kohn anomaly, friedel oscillation, and rky interaction in bilayer graphene, *Phys. Rev. Lett.* **101**, 156802 (2008).
- [55] R. Sensarma, E. H. Hwang, and S. Das Sarma, Dynamic screening and low-energy collective modes in bilayer graphene, *Phys. Rev. B* **82**, 195428 (2010).
- [56] R. Geick, C. H. Perry, and G. Rupprecht, Normal modes in hexagonal boron nitride, *Phys. Rev.* **146**, 543 (1966).
- [57] K. S. Novoselov, E. McCann, S. V. Morozov, V. I. Fal'ko, M. I. Katsnelson, U. Zeitler, D. Jiang, F. Schedin, and A. K. Geim, Unconventional quantum hall effect and berry's phase of 2π in bilayer graphene, *Nature Physics* **2**, 177 (2006).
- [58] See, for example: M Lundstrom, *Fundamentals of Carrier Transport*. Cambridge: Cambridge University Press. (2002).
- [59] E. Mariani and F. von Oppen, Flexural phonons in free-standing graphene, *Phys. Rev. Lett.* **100**, 076801 (2008).
- [60] D. Adinehloo, W. Gao, A. Mojibpour, J. Kono, and V. Perebeinos, Evidence for phonon-assisted intertube electronic transport in an armchair carbon nanotube film, *arXiv:2201.06693* (2022).
- [61] G. Pizzi, S. Milana, A. C. Ferrari, N. Marzari, and M. Gibertini, Shear and breathing modes of layered materials, *ACS Nano* **15**, 12509 (2021).